Asymmetric diffraction by atomic gratings with optical $\mathcal{PT}$ symmetry in the Raman-Nath regime

Tao Shui, Wen-Xing Yang,* Shaopeng Liu, and Ling Li
Department of Physics, Southeast University, Nanjing 210096, China

Zhonghu Zhu
Department of Physics, College of Science, Nanjing Agricultural University, Nanjing 210095, China

(Received 4 September 2017; published 13 March 2018)

We propose and analyze an efficient scheme for the lopsided Raman-Nath diffraction of one-dimensional (1D) and two-dimensional (2D) atomic gratings with periodic parity-time ($\mathcal{PT}$)-symmetric refractive index. The atomic grating is constructed by the cold-atomic vapor with two isotopes of rubidium, which is driven by weak probe field and space-dependent control field. Using experimentally achievable parameters, we identify the conditions under which $\mathcal{PT}$-symmetric refractive index allows us to observe the lopsided Raman-Nath diffraction phenomenon and improve the diffraction efficiencies beyond what is achievable in a conventional atomic grating. The nontrivial atomic grating is a superposition of an amplitude grating and a phase grating. It is found that the lopsided Raman-Nath diffraction at the exceptional point (EP) of $\mathcal{PT}$-symmetric grating originates from constructive and destructive interferences between the amplitude and phase gratings. Furthermore, we show that the $\mathcal{PT}$-phase transition from unbroken to broken $\mathcal{PT}$-symmetric regimes can modify the asymmetric distribution of the diffraction spectrum and that the diffraction efficiencies in the non-negative diffraction orders can be significantly enhanced when the atomic grating is pushed into a broken $\mathcal{PT}$-symmetric phase. In addition, we also analyze the influence of the grating thickness on the diffraction spectrum. Our scheme may provide the possibility to design a gain-beam splitter with tunable splitting ratio and other optical components in integrated optics.

DOI: 10.1103/PhysRevA.97.033819

I. INTRODUCTION

In the past two decades, the study of parity-time ($\mathcal{PT}$) symmetry has been an important interdisciplinary field in the scientific and technological mainstream since the concept of $\mathcal{PT}$ symmetry was first proposed in quantum mechanics by Bender [1,2]. Note that a non-Hermitian Hamiltonian is $\mathcal{PT}$ symmetric and has a real eigenvalue spectrum when it commutes with the $\mathcal{PT}$ operator, i.e., $[H,\mathcal{PT}]=0$. For a general Hamiltonian $H=\hat{p}^2/2m+V(\hat{x})$, with $\hat{p}=i\hbar\partial/\partial t$ in the time-dependent Schrödinger equation $i\hbar\partial\Psi/\partial t=H\Psi$, the action of the space-reflection operator $\mathcal{P}$ and time-reversal operator $\mathcal{T}$ on the momentum and position operators $\hat{p}$ and $\hat{x}$ is $\mathcal{P}$: $\hat{p}\to-\hat{p}$, $\hat{x}\to-\hat{x}$ and $\mathcal{T}$: $\hat{p}\to-\hat{p}$, $\hat{x}\to\hat{x}$, $i\to-i$. Then, $H\mathcal{PT}=\hat{p}^2/2m+V(\hat{x})$ and $\mathcal{PT}H=\hat{p}^2/2m+V^*(-\hat{x})$ can be deduced from the above consideration. Thus, a $\mathcal{PT}$-symmetric Hamiltonian requires $V(\hat{x})=V^*(-\hat{x})$. Unlike the character of a Hermitian Hamiltonian, an exceptional point (EP) exists in the $\mathcal{PT}$-symmetric Hamiltonian with the change of the system parameters. The EP is a phase-transition point corresponding to the phase transition from an unbroken $\mathcal{PT}$-symmetric phase to a broken $\mathcal{PT}$-symmetric phase, where the real eigenvalue spectrum of the $\mathcal{PT}$-symmetric system undergoes a phase-transition start to become complex [2].

In recent years, $\mathcal{PT}$ symmetry has been extended to the field of optics due to the formal equivalence between the paraxial wave equation $[i\partial E(x,z)/\partial z+(2k)^{-1}\partial^2E(x,z)/\partial x^2+k_0n(x)E(x,z)=0]$ and the time-dependent Schrödinger equation [3,4]. The vertical distance z plays the role of time t and the optical Hamiltonian is $H_{\rm opt}=-(2k)^{-1}\partial^2/\partial x^2-k_0n(x)$ [5]. Then, the action of the operators $\mathcal{P}$ and $\mathcal{T}$ on the transverse position x is $\mathcal{P}$: $x\to-x$ and $\mathcal{T}$: $x\to x$, $i\to-i$. In this situation, we can deduce $H_{\rm opt}\mathcal{PT}=-(2k)^{-1}\partial^2/\partial x^2-k_0n(x)$ and $\mathcal{PT}H_{\rm opt}=-(2k)^{-1}\partial^2/\partial x^2-k_0n^*(-x)$, where the complex refractive index $n(x)=n_r(x)+in_i(x)$ is equivalent to the potential $V(\hat{x})$. Thus, the condition of an optical system being $\mathcal{PT}$ symmetric is $n(x)=n^*(-x)$. This relation indicates that the real part $n_r(x)$ of the complex refractive index must be an even function of x, whereas the imaginary component $n_i(x)$, i.e., gain and absorption, should be odd in optical $\mathcal{PT}$ symmetry. Numerous optical $\mathcal{PT}$-symmetric systems relying on the modulations of gain and absorption have been theoretically and experimentally realized in synthetic waveguides [3,5–9], photonic lattices [4,10–13], microcavities [14–19], and cold-atom gases [20–25]. Meanwhile, many novel optical phenomena have been discovered, such as Bloch oscillation [10,11], single-mode laser [15], ultralow-threshold chaos [16], enhanced high-order sideband [18,19], coherent perfect absorbers [13,22], Gaint Goos-Hänchen shift [25], nonreciprocal and unidirectional light propagation [8,26,27], and asymmetric Bragg diffraction [28–31].

On the other hand, much attention has been attracted to the field of grating diffraction due to its significant applications in the fields of natural science and industrial production [32–36].

*wenxingyang2@126.com

As an optical component with periodic structure, the grating can diffract the incident light beam into a high-order diffraction direction. To our knowledge, the prototype of diffraction grating was first made by Rittenhouse in 1785 [32]. He constructed a half-inch-wide grating with 53 apertures. Since then, a lot of schemes have been proposed to study the diffraction characteristics and applications of ruled gratings [37], holographic grating [38–41], silicon gratings [34,35], and metal gratings [42]. In recent years, based on electromagnetically induced transparency (EIT) [43], the tunable atomic gratings called electromagnetically induced gratings (EIGs) have been theoretically and experimentally investigated in multilevel atomic vapors [44–54]. The notable point in these investigations is that a standing-wave field replacing the traveling-wave field of EIT can modulate the spatial distribution of the refractive index, gain-absorption coefficient, or both of the atomic medium, thereby forming an atomic grating.

It is worth noting that the plane diffraction gratings operate in two different diffraction regimes: Bragg regime (or thick grating) [33,38,50,51,55,56] and Raman-Nath regime (or thin grating) [33,39–41,44–49,57]. In the Bragg regime, essentially only two waves, i.e., one transmitted wave and one diffracted wave, exist when the light wave is incident at or near the Bragg angle [38], while multiple diffraction waves are generated in the Raman-Nath regime [33]. Note that a criterion has been introduced to distinguish between the two diffraction regimes [58]. We notice that the phenomena of Bragg diffraction in thick gratings [30] and photonic crystal [31] with $\mathcal{PT}$-symmetric optical potential have recently been investigated. It has been shown that by introducing the spatial modulations of the refractive index and gain and absorption with a $\pi/2$ phase shift between them, the $\mathcal{PT}$ symmetry can result in asymmetric diffraction when the sign of the Bragg incident angle is changed. As we know, the $\mathcal{PT}$-symmetric systems [20–25] and atomic gratings [44–54] induced by atomic coherence in the atomic vapors can be actively and effectively controlled via adjusting the optical parameters of the system, such as the intensities and detunings of the applied fields. Thus, it reminds us of one question: could some new Raman-Nath diffraction characteristics occur in the atomic grating with a $\mathcal{PT}$-symmetric refractive index?

In this paper, we investigate the spectrum characteristics of Raman-Nath diffraction in one-dimensional (1D) and 2D atomic gratings with a periodic $\mathcal{PT}$-symmetric refractive index. Our proposal is motivated by the earlier research about weak-light solitons in a $\mathcal{PT}$-symmetric atomic system, which is formed by the interference of two Raman resonances [21]. The continuously tunable atomic grating consists of a phase grating with cosinoidal phase modulation and an amplitude grating with sinusoidal gain-absorption modulation. We demonstrate that the gain-absorption modulation plays an important role in the spatial distribution of Raman-Nath diffraction spectra in one and two dimensions. Different from the diffraction spectra in the conventional atomic gratings [44–49], the proposed atomic grating presents an asymmetric diffraction effect in one and two dimensions when the modulated refractive index satisfies $\mathcal{PT}$ symmetry. Using the interference mechanism between the phase grating and the amplitude grating [39,40], we can give the physical interpretation of the asymmetry diffraction phenomenon. Our results illustrate that the lopsided diffraction spectra stimulated by 1D and 2D atomic gratings can be achieved at the EP. Moreover, the diffraction efficiencies in the non-negative diffraction orders can be significantly enhanced when the atomic grating is pushed into a broken $\mathcal{PT}$-symmetric phase. In the $\mathcal{PT}$-phase region, we investigate the influence of the grating thickness on the diffraction spectrum. It is found that the increase of the grating thickness in the Raman-Nath regime can stimulate higher diffraction orders and result in a redistribution of the diffraction efficiencies. More importantly, the thickness of the atomic grating cannot affect the zeroth-order diffraction field when the atomic grating is at the EP. Based on these results, the atomic grating with a $\mathcal{PT}$-symmetric refractive index may potentially have the functions of optical beam deflecting, sampling, shaping, and splitting with ultrahigh diffraction efficiency.

II. MODEL AND METHOD

We consider a mixed system of two isotopes (^{87}Rb and ^{85}Rb) of cold-atomic rubidium. As shown in Fig. 1(a), the energy-level structure of each isotope is treated as a three-level Λ-type configuration with an excited state $|a,m\rangle$ and two ground states $|b,m\rangle$ and $|c,m\rangle$ ($m = 1,2$ is the

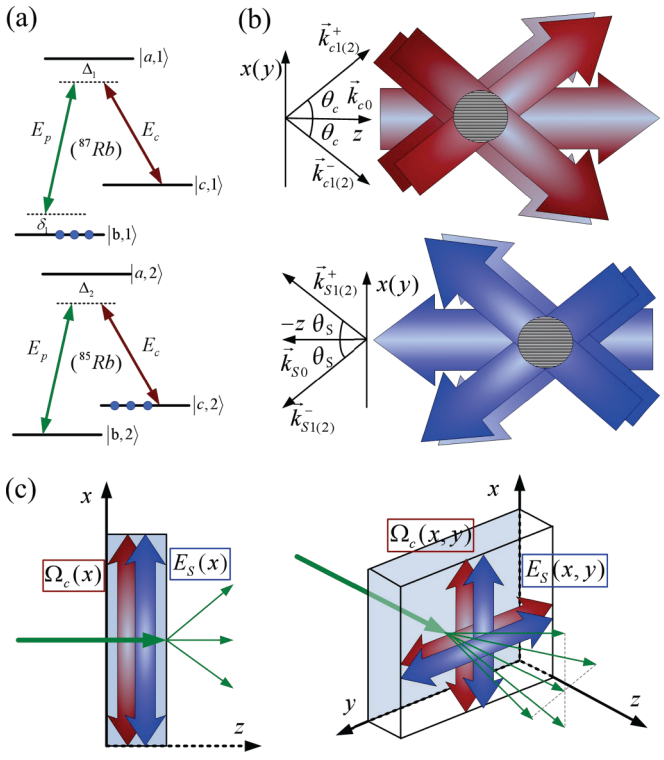

FIG. 1. (a) Schematic diagram for a mixed system of two species of cold ^{87}Rb and ^{85}Rb atoms with three-level Λ-type structure, in which blue dots indicate the initial populated level. (b) Possible experimental setup of the position-dependent control field (red arrow) E_c and Stark field (blue arrow) E_S, each of which consists of a z-direction optical beam (E_{c0} or E_{S0}) and two pairs of optical beams ($E^{\pm}_{cj}$ or $E^{\pm}_{Sj}$, $j = 1,2$) with cross angle (θ_c or θ_S). The striation area is the region of spatial modulation. (c) Sketch of 1D and 2D electromagnetically induced grating in the cold-atomic sample.

species of the atoms). Such a mixed atomic system can be realized in the mixture of cold ^{87}Rb (species 1) and ^{85}Rb (species 2) atoms using the D1 line. The designated states can be chosen as follows: $|a,1\rangle = |5\,^2P_{1/2}, F = 1\rangle$, $|b,1\rangle = |5\,^2S_{1/2}, F = 1\rangle$, $|c,1\rangle = |5\,^2S_{1/2}, F = 2\rangle$ for the ^{87}Rb atom, and $|a,2\rangle = |5\,^2P_{1/2}, F = 2\rangle$, $|b,2\rangle = |5\,^2S_{1/2}, F = 2\rangle$, $|c,2\rangle = |5\,^2S_{1/2}, F = 3\rangle$ for the ^{85}Rb atom. A weak probe field E_p with half Rabi frequency $\Omega_{pm} = \vec{\mu}^{\,m}_{ab} \cdot \vec{e}_{\,p} E_p/2\hbar$ (frequency ω_p) couples to the transition $|a,m\rangle \to |b,m\rangle$ (resonant frequency ω^m_{ab}), while the transition $|a,m\rangle \to |c,m\rangle$ (resonant frequency ω^m_{ac}) is driven by a control field E_c with half Rabi frequency $\Omega_{cm} = \vec{\mu}^{\,m}_{ac} \cdot \vec{e}_{\,c} E_c/2\hbar$ (frequency ω_c). $\vec{\mu}^{\,m}_{ab}$ ($\vec{\mu}^{\,m}_{ac}$) presents the electric-dipole matrix moment for the relevant optical transitions from state $|a,m\rangle$ to state $|b,m\rangle$ ($|c,m\rangle$), with $\vec{e}_{\,p}$ ($\vec{e}_{\,c}$) denoting the unit polarization vector of the probe (control) field. For the selected levels of two isotopes of rubidium, the dipole matrix moments are assumed to be approximately equal and $\mu^m_{ab} \approx \mu^m_{ac} = 2.5377 \times 10^{-29}$ C m [59]. For simplicity, $\Omega_{p1} = \Omega_{p2} = \Omega_p$ and $\Omega_{c1} = \Omega_{c2} = \Omega_c$.

Under the electric-dipole and rotating-wave approximations, the resulting interaction Hamiltonian for each subsystem ($m = 1,2$) in the interaction picture can be written as

$$H^m_I = \hbar \begin{pmatrix} \Delta_m + \delta_m & -\Omega_c & -\Omega_p \\ -\Omega^*_c & \delta_m & 0 \\ -\Omega^*_p & 0 & 0 \end{pmatrix}, \tag{1}$$

where $\Delta_m = \omega^m_{ac} - \omega_c$ and $\delta_m = \omega^m_{ab} - \omega^m_{ac} - (\omega_p - \omega_c)$ are the one- and two-photon detunings. The dynamics of the subsystem ($m = 1,2$) can be described by using the density matrix approach as

$$\frac{d\rho^m}{dt} = -\frac{i}{\hbar}\left[H^m_I, \rho^m\right] + L[\rho^m(t)]. \tag{2}$$

Here, the Liouvillian matrix $L[\rho^m(t)]$ indicating the relaxation by spontaneous decay can be written as

$$L[\rho^m(t)] = \begin{pmatrix} -\left(\Gamma^m_{ab} + \Gamma^m_{ac}\right)\rho^m_{aa} & -\gamma^m_{ac}\rho^m_{ac} & -\gamma^m_{ab}\rho^m_{ab} \\ -\gamma^m_{ac}\rho^m_{ca} & \Gamma^m_{ac}\rho^m_{aa} & -\gamma^m_{cb}\rho^m_{cb} \\ -\gamma^m_{ab}\rho^m_{ba} & -\gamma^m_{cb}\rho^m_{bc} & \Gamma^m_{ab}\rho^m_{aa} \end{pmatrix}, \tag{3}$$

where the coherence decay rates are defined as $\gamma^m_{ab} = (\Gamma^m_{ab} + \Gamma^m_{ac} + \gamma^m_{a,deph})/2$, $\gamma^m_{ac} = (\Gamma^m_{ab} + \Gamma^m_{ac} + \gamma^m_{a,deph} + \gamma^m_{c,deph})/2$, and $\gamma^m_{cb} = (\Gamma^m_{cb} + \gamma^m_{c,deph})/2$, in which Γ^m_{ij} $(i,j = a,b,c)$ is the spontaneous-emission decay rate from state $|i,m\rangle$ to state $|j,m\rangle$ and $\gamma^m_{a,deph}$ and $\gamma^m_{c,deph}$ are phenomenological decay rates that model the energy-conserving dephasing processes. Γ^m_{cb} is much smaller than Γ^m_{ab} (Γ^m_{ac}) and, consequently, can be neglected, that is, $\Gamma^m_{cb} \simeq 0$. As the ^{87}Rb ($m = 1$) and ^{85}Rb ($m = 2$) atoms are loaded into a cell at low temperature ($\sim\mu$K), $\Gamma^m_{ab} \simeq \Gamma^m_{ac} = \Gamma = \pi \times 5.75$ MHz and dephasing processes can be safely neglected [59]. As a result, $\gamma^m_{ab} = \gamma^m_{ac} = \Gamma$ and $\gamma^m_{cb} = 0$.

In our mixed system, the sum of the susceptibility from each subsystem forms the total complex susceptibility. Therefore, the total susceptibility of the weak probe field can be defined by

$$\chi_p = \frac{|\mu_{ab}|^2}{\epsilon_0 \hbar \Omega_p}\left(N_1 \rho^1_{ab} + N_2 \rho^2_{ab}\right), \tag{4}$$

where N_1 and N_2 are the atom number densities of isotopes ^{87}Rb and ^{85}Rb in the cell, respectively.

In the proposed scheme, we consider the case that the ^{87}Rb (^{85}Rb) atom is initially prepared in ground state $|b,1\rangle$ ($|c,2\rangle$), i.e., $\rho^1_{bb}(0) = \rho^2_{cc}(0) = 1$, which is achieved by locking two additional optical pumping lasers to the $|c,1\rangle \to |a,1\rangle$ transition for ^{87}Rb and the $|b,2\rangle \to |a,2\rangle$ transition for ^{85}Rb [not indicated in Fig. 1(a)] before the probe and control fields are turned on [60]. Similar to Refs. [61,62], we have assumed that probe field E_p is sufficiently weak and the detuning between the control (probe) field and the transition $|a,m\rangle \to |c,m\rangle$ ($|a,m\rangle \to |b,m\rangle$) is sufficiently large. Therefore, the atomic population depletions of the ground states $|b,1\rangle$ (for ^{87}Rb) and $|c,2\rangle$ (for ^{85}Rb) can be neglected in the presence of sufficiently strong optical lasers. It means that most of the atomic population remains in ground states $|b,1\rangle$ (for ^{87}Rb) and $|c,2\rangle$ (for ^{85}Rb), i.e., $\rho^{1(ss)}_{bb} \simeq \rho^{2(ss)}_{cc} \simeq 1$ [superscript (ss) represents the steady state]. In this situation, the weak probe field can be absorbed by the ^{87}Rb atom and amplified by the ^{85}Rb atom in the stimulated Raman transition $|c,m\rangle \to |b,m\rangle$ ($m = 1,2$). Meanwhile, the two-photon detuning δ_2 of the ^{85}Rb atom is taken as zero via adjusting the frequency ω_p of the probe field without taking into account the effect of Doppler broadening in the ensemble of cold atoms. The required density matrix elements ρ^1_{ab} and ρ^2_{ab} can be obtained by solving Eqs. (1)–(3). Consequently, by using perturbation theory in the limit of weak probe field, the analytical expression for χ_p in the steady state can be written as [21]

$$\chi_p = \frac{|\mu_{ab}|^2}{\epsilon_0 \hbar}\left(\frac{N_1 \delta_1}{\delta_1^2 + \delta_1 \Delta_1 - i\delta_1 \Gamma - |\Omega_c|^2} + \frac{N_2}{\Delta_2 + i\Gamma}\right). \tag{5}$$

Note that the real and imaginary parts of the complex susceptibility, i.e., $\chi_p = \chi'_p + i\chi''_p$, determine the real and imaginary parts of the complex refractive index $n = \sqrt{1 + \chi_p} = n_r + i n_i$. Thus, Eq. (5) gives the following expressions of the real and imaginary parts of the susceptibility:

$$\chi'_p = \frac{N_1 |\mu_{ab}|^2}{\epsilon_0 \hbar}\left\{\frac{\delta_1\left[\delta_1^2 + \delta_1 \Delta_1 - |\Omega_c|^2\right]}{\left[\delta_1^2 + \delta_1 \Delta_1 - |\Omega_c|^2\right]^2 + \delta_1^2 \Gamma^2} + \frac{\eta \Delta_2}{\Delta_2^2 + \Gamma^2}\right\},$$
$$\chi''_p = \frac{N_1 |\mu_{ab}|^2}{\epsilon_0 \hbar}\left\{\frac{\delta_1^2 \Gamma}{\left[\delta_1^2 + \delta_1 \Delta_1 - |\Omega_c|^2\right]^2 + \delta_1^2 \Gamma^2} - \frac{\eta \Gamma}{\Delta_2^2 + \Gamma^2}\right\}, \tag{6}$$

where $\eta = N_2/N_1$.

The realization of $\mathcal{PT}$-symmetric probe-field susceptibility, i.e., $\chi_p(\mathbf{x}) = \chi^*_p(-\mathbf{x})$ (and hence the $\mathcal{PT}$ refractive index $n(\mathbf{x}) = [1 + \chi_p(\mathbf{x})]^{1/2} = [1 + \chi^*_p(-\mathbf{x})]^{1/2} = n^*(-\mathbf{x})$), relies on the spatial modulations of the control field $E_c(\mathbf{x})$ [Rabi frequency $\Omega_c(\mathbf{x})$] and one-photon detuning $\Delta_m(\mathbf{x})$ ($m = 1,2$) in Eq. (6). Here, $\mathbf{x}$ is the transverse coordinate in space. The position-dependent detuning $\Delta_m(\mathbf{x})$ originates from the Stark effect, which is the shifting of spectrum lines of atoms. A far-off-resonant Stark field with the amplitude of the electric field $E_S(\mathbf{x})$ and the wavelength λ_S will induce a space-modulated

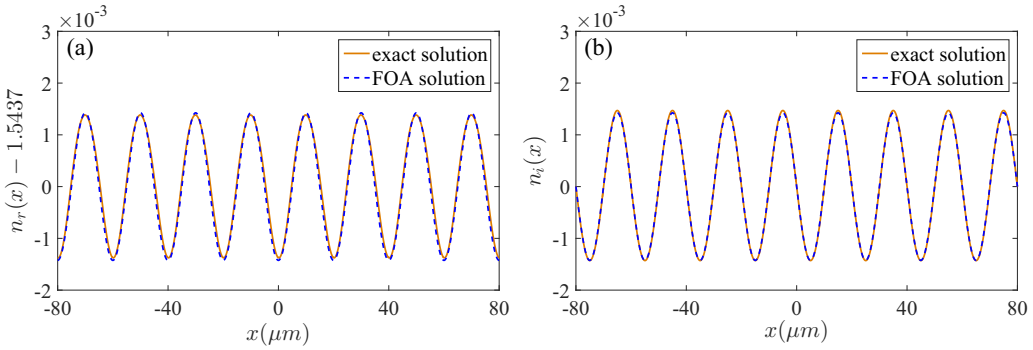

FIG. 2. (a) The real part $n_r(x)$ and (b) the imaginary part $n_i(x)$ of the 1D complex refractive index as functions of x. Solid orange lines in (a) and (b) show the exact solution of the complex refractive index, while dashed blue lines represent the corresponding first-order approximate (FOA) solution of the exact refractive index. The other parameters are $\Delta_1 = 8\Gamma$, $\Delta_2 = 8.72\Gamma$, $\delta_1 = 1.81\Gamma$, $\Lambda = 20\ \mu$m, $V_0 = 3$, and $W_0 = 1.5$.

energy shift $\triangle E_j^m(\mathbf{x}) = -\alpha_j^m E_S^2(\mathbf{x})/4$ (α_j^m is the corresponding scalar polarizability) for level $|j,m\rangle$ in the two species ($m = 1,2$). For the selected D1 line ($5\,^2S_{1/2} \rightarrow 5\,^2P_{1/2}$) of isotopes ^{87}Rb ($m = 1$) and ^{85}Rb ($m = 2$), the ground-state polarizability $\alpha_b^m \simeq \alpha_c^m = 2\pi\hbar \times 0.0794$ Hz/(V/cm)^2 and the D1 scalar polarizability $\alpha_a^m - \alpha_b^m = 2\pi\hbar \times 0.1223$ Hz/(V/cm)^2 [59]. Ignoring the difference of Stark shifts between level $|b,m\rangle$ and level $|c,m\rangle$, the Stark field cannot affect the two-photon detuning δ_1. However, it can amend the one-photon detuning, i.e., $\Delta_m(\mathbf{x}) = \Delta_m - (\alpha_a^m - \alpha_b^m)E_S(\mathbf{x})^2/4\hbar$, where Δ_m is one-photon detuning in the absence of the Stark field.

Notice that $\mathcal{PT}$ symmetry requires $\chi_p''(\mathbf{x})$ to be an odd function, hence the imaginary part of the susceptibility is zero at $\mathbf{x} = 0$ and we then obtain the relationship between N_1 and N_2 as

$$\eta = \frac{N_2}{N_1} = \frac{\delta_1^2\left[\Delta_2^2(0) + \Gamma^2\right]}{\left[\delta_1^2 + \delta_1\Delta_1^2(0) - |\Omega_c(0)|^2\right] + \delta_1^2\Gamma^2}. \quad (7)$$

By taking 1D spatial-dependent susceptibility as an example, we introduce the approach to construct a $\mathcal{PT}$-symmetric optical potential as follows: First, we define a seed susceptibility $\chi_p^{sd} = \chi_{p0} - \chi_{p1}\cos(Kx) - i\chi_{p2}\sin(Kx)$, where χ_{pj} ($j = 0,1,2$) is the free parameter. Second, we compute analytical solutions for real $\Omega_c^{sd}(x,\chi_{pj},\eta)$ and $E_S^{sd}(x,\chi_{pj},\eta)$ by solving equation $\chi_p(\Omega_c^{sd},E_S^{sd}) = \chi_p^{sd}$. Third, we substitute Ω_c^{sd} and E_S^{sd} back into Eq. (6) and make the error function $\varsigma(x) = n(x) - n^*(-x)$ as small as possible by tuning the parameters χ_{pj} and η. Since the expressions of $\Omega_c(x)$ and $E_S(x)$ are fairly complex, we can keep the first significant harmonics (i.e., the terms $\geqslant 10^{-3}$) for the final expressions of $\Omega_c(x)$ and $E_S(x)$. Because there is a slight difference between the final susceptibility $\chi_p(x)$ and the seed susceptibility χ_p^{sd}, the real and imaginary parts of the susceptibility can be represented by a Fourier series in which the first significant harmonics is kept (for more details, see [20]).

In the following, the parameters $\Delta_1 = 8\Gamma$, $\Delta_2 = 8.72\Gamma$, $\delta_1 = 1.81\Gamma$, $\lambda_p \simeq 0.658\ \mu$m, and $\lambda_S \simeq 5\ \mu$m are chosen. Here, the wavelength of the Stark field is so long that no quantum interference exists between the Stark field and the atomic system. Thus, the Stark field only causes energy shift and has no influence on the stimulated Raman process. In experiment, the Stark field in the midinfrared range can be generated by a quantum cascade laser working at continuous-wave operation [63]. In addition, we select $N_1 \simeq 7.86 \times 10^{13}$ cm^{-3} based on Eq. (5), which leads to $N_1|\mu_{ab}|^2/\epsilon_0\hbar \sim 3$.

For 1D $\mathcal{PT}$-symmetric susceptibility, i.e., $\chi_p(x) = \chi_p^*(-x)$, as shown in Fig. 1(b), the Stark field $E_S(x)$ [or the control field $E_c(x)$] consists of a z-direction laser field E_{S0} (or E_{c0}) and two pairs of laser fields $E_{S1}^{\pm}$ and $E_{S2}^{\pm}$ (or $E_{c1}^{\pm}$ and $E_{c2}^{\pm}$) with cross angle θ_S (or θ_c), in which each pair of laser fields can form a standing wave along the x direction. In this case, we define two undetermined modulation factors V_0 and W_0, which can feature different regions of an optical $\mathcal{PT}$-symmetric system. When $\eta = 2.1541$ is confirmed and both the Stark field and the control field satisfy Eq. (A2) in the Appendix, by keeping the first significant harmonics, the real and imaginary parts of the first-order approximate (FOA) susceptibility in Eq. (6) are given as follows:

$$\begin{aligned}\chi_p'(x) &= 1.383 - 0.0015V_0\cos(Kx),\\ \chi_p''(x) &= -0.003W_0\sin(Kx),\end{aligned} \quad (8)$$

where $K = 2\pi/\Lambda$ and Λ is the period of standing waves.

One can find from Eqs. (A2) and (8) that the spatial intensities of the Stark field $E_S(x)$ and the control field $\Omega_c(x) = \vec{\mu}_{ac}\cdot\vec{e}_c E_c(x)/2\hbar$ determine the values of V_0 and W_0, and hence determine the $\mathcal{PT}$-symmetric probe susceptibility. Here, the parameters V_0 and W_0 provide a possibility of continuously adjusting $\mathcal{PT}$ symmetry via changing the intensity distributions of both the Stark field and the control field. The space-dependent susceptibility in Eq. (8) further leads to the 1D $\mathcal{PT}$-symmetric refractive index $n(x) = [1 + \chi_p'(x) + i\chi_p''(x)]^{1/2} = [\varepsilon_0 - \varepsilon_1\cos(Kx) - i\varepsilon_2\sin(Kx)]^{1/2}$, in which $\varepsilon_0 = 2.383$, $\varepsilon_1 = 0.0015V_0$, and $\varepsilon_2 = 0.003W_0$. In the sufficiently small modulation ($\varepsilon_0 \gg \varepsilon_1,\varepsilon_2$), the 1D $\mathcal{PT}$-symmetric refractive index can be written as [33]

$$\begin{aligned}n(x) &= n_r(x) + in_i(x)\\ &= n_0 - n_1\cos(Kx) - in_2\sin(Kx),\end{aligned} \quad (9)$$

with $n_0 = \varepsilon_0^{1/2} = 2.383^{1/2}$, $n_1 = \varepsilon_1/2\varepsilon_0^{1/2} = 0.00075V_0/2.383^{1/2}$, and $n_2 = 0.0015W_0/2.383^{1/2}$.

To show the accuracy of the $\mathcal{PT}$-symmetric optical potential realized by the above approach, we substitute Eqs. (A2) into (6) and then, using $n(x) = [1 + \chi_p'(x) + i\chi_p''(x)]^{1/2}$, plot the real and imaginary parts of the refractive index with and without approximation as functions of x in Figs. 2(a)

and 2(b) for $\Delta_1 = 8\Gamma, \Delta_2 = 8.72\Gamma, \delta_1 = 1.81\Gamma, \Lambda = 20\ \mu$m, $V_0 = 3$, and $W_0 = 1.5$. When the Stark field and control field in Eq. (A2) are selected, one can find that the exact refractive index [see solid orange lines in Figs. 2(a) and 2(b)] coincides well with the first-order approximate (FOA) solution, which keeps the first significant harmonics of the Fourier series development of the refractive index [see dashed blue lines in Figs. 2(a) and 2(b)]. The real and imaginary parts of the exact refractive index are almost modulated with the cosine function and sine function, respectively. Thus, the above approach to realize a $\mathcal{PT}$-symmetric optical system is valid.

For 2D $\mathcal{PT}$-symmetric susceptibility, i.e., $\chi_p(x,y) = \chi_p^*(-x,-y)$, we can extend $E_s(x)$ and $\Omega_c(x)$ in Eq. (A2) into 2D forms $E_s(x,y)$ and $\Omega_c(x,y)$ by adding two pairs of Stark fields ($E_{S3}^{\pm}$, $E_{S4}^{\pm}$) and control fields ($E_{c3}^{\pm}, E_{c4}^{\pm}$) with cross angles θ_S and θ_c, respectively. In this case, E_{mn}^{+} and E_{mn}^{-} ($m = c,S; n = 3,4$) form a standing wave along the y direction with an initial phase ϕ_{mn}. When the condition in Eq. (A3) is satisfied, the real and imaginary parts of the $\mathcal{PT}$-symmetric susceptibility in two dimensions are given by

$$\begin{aligned}\chi_p'(x,y) &= 1.383 - 0.0015V_0[\cos(Kx) + \cos(Ky)],\\ \chi_p''(x,y) &= -0.003W_0[\sin(Kx) + \sin(Ky)],\end{aligned} \tag{10}$$

which further results in the 2D $\mathcal{PT}$-symmetric refractive index $n(x,y) = [1 + \chi_p'(x,y) + i\chi_p''(x,y)]^{1/2} = \{\varepsilon_0 - \varepsilon_1[\cos(Kx) + \cos(Ky)] - i\varepsilon_2[\sin(Kx) + \sin(Ky)]\}^{1/2}$ with $\varepsilon_0 = 2.383$, $\varepsilon_1 = 0.0015V_0$, and $\varepsilon_2 = 0.003W_0$. In the sufficiently small modulation, the 2D $\mathcal{PT}$-symmetric refractive index can be written as

$$\begin{aligned}n(x,y) = n_0 &- n_1[\cos(Kx) + \cos(Ky)]\\ &- in_2[\sin(Kx) + \sin(Ky)],\end{aligned} \tag{11}$$

where $n_0 = \varepsilon_0^{1/2}$, $n_1 = \varepsilon_1/2\varepsilon_0^{1/2}$, and $n_2 = \varepsilon_2/2\varepsilon_0^{1/2}$.

Therefore, the periodic modulation of the complex refractive index in Eqs. (9) and (11) can form 1D and 2D atomic grating. In what follows, we introduce two methods to investigate the Raman-Nath diffraction characteristics of 1D and 2D atomic gratings with $\mathcal{PT}$-symmetric optical potential, as shown in Fig. 1(c). The first method is the amplitude transmittance approach used to give the 1D and 2D diffraction spectrum through Fourier transform for the transmission function [44]. The second method is using the coupled-wave theory of Raman-Nath regime diffraction to analytically give the diffraction efficiency of each diffraction order [33].

In the atomic grating with $\mathcal{PT}$-symmetric refractive index $n(\mathbf{x})$, the weak probe field propagating along the z direction in the $\mathcal{PT}$-symmetric grating is written as

$$E(\mathbf{x},z) = E_p(\mathbf{x},z)e^{-i\beta z}, \tag{12}$$

in which $\beta = k_0 n_0$ is the effective propagation constant in the atomic medium and $k_0 = 2\pi/\lambda_p$ indicates the propagation constant in free space. In addition, the amplitude of the wave E_p varies slowly in space. The propagation of the probe field in the atomic grating satisfies the wave equation:

$$\nabla^2 E(\mathbf{x},z) + k_0^2 n^2(\mathbf{x})E(\mathbf{x},z) = 0. \tag{13}$$

Figure 1(c) shows the sketch of 1D and 2D atomic grating induced by atomic coherence in the cold-atomic sample. For the 1D $\mathcal{PT}$-symmetric refractive index, substituting $n(\mathbf{x}) = n(x)$ and $E(\mathbf{x},z) = E(x,z) = E_p(x,z)e^{-i\beta z}$ into the wave equation (13), we then leave out the fact $e^{-i\beta z}$ and obtain the resulting wave equation under a slowly varying envelope approximation (SVEA) as follows:

$$-2i\beta\frac{\partial E_p}{\partial z} = 2k_0^2 n_0[n_1\cos(Kx) + in_2\sin(Kx)]E_p. \tag{14}$$

Then, Eq. (14) becomes

$$\frac{\partial E_p}{\partial z} = \frac{2\pi}{\lambda_p}[in_1\cos(Kx) - n_2\sin(Kx)]E_p. \tag{15}$$

Here, we assume that the interaction length between the isotopes (^{87}Rb and ^{85}Rb) and probe field along the z direction, i.e., the grating thickness, is L. Meanwhile, the amplitude transmission is defined as the ratio of the output field amplitude at $z = L$ to the input field amplitude at $z = 0$. Due to the amplitude modulation and phase modulation in the x direction, the amplitude transmission function is given by

$$T(x) = e^{-\alpha_1(x)L}e^{i\alpha_2(x)L}, \tag{16}$$

where $\alpha_1(x) = 2\pi n_2\sin(Kx)/\lambda_p$ and $\alpha_2(x) = 2\pi n_1\cos(Kx)/\lambda_p$ are the spatial modulations of the amplitude and phase, respectively.

In the case of far-field Fraunhofer diffraction, the diffraction spectrum of the weak probe field is obtained by the Fourier transform of the amplitude transmission function $T(x)$. The normalized diffraction intensity function can be written as

$$I_p(\theta) = |F(\theta)|^2\frac{\sin^2(N\pi\Lambda\sin\theta/\lambda_p)}{N^2\sin^2(\pi\Lambda\sin\theta/\lambda_p)}, \tag{17}$$

where θ indicates the diffraction angle with respect to the z direction and N represents the number of spatial periods of the atomic grating illuminated by the probe field. $F(\theta)$ is the Fraunhofer diffraction of a single space period Λ, which is given by

$$F(\theta) = \frac{1}{\Lambda}\int_0^{\Lambda} T(x)e^{-i2\pi x\sin\theta/\lambda_p}dx. \tag{18}$$

In particular, if the condition of $\sin\theta_m = m\lambda_p/\Lambda$ is satisfied, the diffraction intensity I_m along the mth-order diffraction direction can be calculated by

$$I_m = I_p(\theta_m) = |F(\theta_m)|^2, \tag{19}$$

with $F(\theta_m) = (1/\Lambda)\int_0^{\Lambda} T(x)e^{-i2\pi mx/\Lambda}dx$.

In a similar way, 2D amplitude transmission function $T(x,y)$ of the probe field in 2D atomic grating with $\mathcal{PT}$-symmetric refractive index $n(x,y)$ can be obtained as

$$T(x,y) = e^{-\alpha_1(x,y)L}e^{i\alpha_2(x,y)L}, \tag{20}$$

with $\alpha_1(x,y) = 2\pi n_2[\sin(Kx) + \sin(Ky)]/\lambda_p$ and $\alpha_2(x,y) = 2\pi n_1[\cos(Kx) + \cos(Ky)]/\lambda_p$.

In the region of Fraunhofer diffraction, the 2D diffraction spectrum of the weak probe field is obtained by the 2D Fourier transform of the amplitude transmission function $T(x,y)$. And then the diffraction-intensity function can be written as

$$\begin{aligned}I_p(\theta_x,\theta_y) = |F(\theta_x,\theta_y)|^2&\frac{\sin^2(N_x\pi\Lambda\sin\theta_x/\lambda_p)}{N_x^2\sin^2(\pi\Lambda\sin\theta_x/\lambda_p)}\\ &\times\frac{\sin^2(N_y\pi\Lambda\sin\theta_y/\lambda_p)}{N_y^2\sin^2(\pi\Lambda\sin\theta_y/\lambda_p)},\end{aligned} \tag{21}$$

where $\theta_{x(y)}$ is the diffraction angle with respect to the z direction in the $x(y)-z$ plane and $N_{x(y)}$ stands for the number of spatial periods of the $\mathcal{PT}$-symmetric grating along the $x(y)$ direction. The Fraunhofer diffraction $F(\theta_x,\theta_y)$ of a single space period Λ in 2D space is given by

$$F(\theta_x,\theta_y) = \frac{1}{\Lambda^2}\int_0^{\Lambda} dx e^{-i2\pi x \sin\theta_x/\lambda_p} \times \int_0^{\Lambda} T(x,y) e^{-i2\pi y \sin\theta_y/\lambda_p} dy. \quad (22)$$

When both $\sin\theta_x^m = m\lambda_p/\Lambda$ and $\sin\theta_y^n = n\lambda_p/\Lambda$ are satisfied, we can obtain the diffraction intensity $I_{(m,n)}$ along the (m,n)th-order diffraction direction as

$$I_{(m,n)} = F\left(\theta_x^m,\theta_y^n\right) = \left|\frac{1}{\Lambda^2}\int_0^{\Lambda} dx e^{-i2\pi mx/\Lambda} \times \int_0^{\Lambda} T(x,y) e^{-i2\pi ny/\Lambda} dy\right|^2. \quad (23)$$

Next, we give the coupled-wave analysis of Raman-Nath diffraction in the 1D and 2D atomic gratings. Based on Eqs. (12) and (13), the propagation constant $k_0 n(x)$ inside 1D atomic grating in the $\mathcal{PT}$-phase regime satisfies

$$\begin{aligned} k_0^2 n^2(x) &= k_0^2[n_0 - n_1\cos(Kx) - in_2\sin(Kx)]^2 \\ &= k_0^2\{n_0^2 - 2n_0[n_1\cos(Kx) + in_2\sin(Kx)]\} \\ &= \beta^2 - 2\beta[\kappa^+ e^{iKx} + \kappa^- e^{-iKx}], \end{aligned} \quad (24)$$

where we neglect the second-order small quantity, i.e., $n_1 n_2$, and the coupling constant $\kappa^{\pm}$ can be defined as

$$\kappa^{\pm} = \frac{\pi(n_1 \pm n_2)}{\lambda_p} = \frac{0.0015\pi(0.5V_0 \pm W_0)}{2.383^{1/2}\lambda_p}, \quad (25)$$

which is different from the case in conventional planar transmission grating for $W_0 > 0$. The coupling constants κ^+ and κ^- in the conventional grating are identical. Furthermore, they have a positive real value for phase grating with cosinusoidal modulated phase grating.

For the 1D $\mathcal{PT}$-symmetric periodic optical potential with the complex refractive index $n(x) = n_0 - n_1\cos(Kx) - in_2\sin(Kx)$, an exceptional point (EP) corresponding to a phase transition from unbroken to broken $\mathcal{PT}$ symmetry occurs at $n_1 = n_2$, that is, $W_0 = W_c = 0.5V_0$. When $W_0 < W_c$, there is a band gap between two real energy bands in the periodic lattice and the eigenvalues are real, which corresponds to unbroken $\mathcal{PT}$ symmetry. As W_0 is increased close to W_c, the band gap of the lattice shrinks until a gapless energy spectrum is obtained at the EP. Two energy bands begin to become complex and pairs of complex conjugate eigenvalues begin to appear, which corresponds to broken $\mathcal{PT}$ symmetry (see, for instance, [27]). Consequently, based on Eq. (25), we can find different characteristics of the coupling constant $\kappa^{\pm}$ for three different phase regions: unbroken $\mathcal{PT}$-symmetric phase (UPTP), EP phase, and broken $\mathcal{PT}$-symmetric phase (BPTP). In Fig. 3, we present the dependence of the coupling constants $\kappa^{\pm}$ on the parameter W_0, which describes the balanced gain and absorption in the atomic grating. The coupling constant κ^+ in the positive direction increases as the parameter W_0 monotonously increases (see solid orange line in Fig. 3),

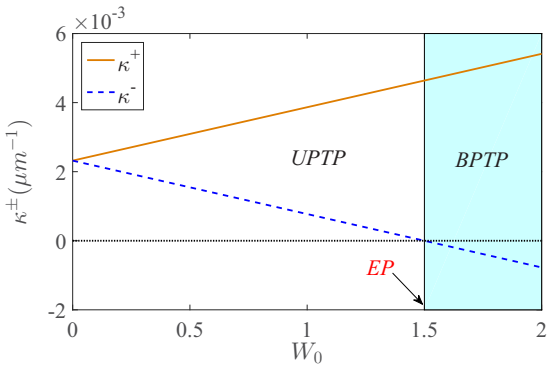

FIG. 3. The coupling constant $\kappa^{\pm}$ as a function of the parameter W_0, which describes the balanced gain and loss. The other parameters are $\lambda_p \simeq 0.658$ μm and $V_0 = 3$.

while the negative-direction coupling constant κ^- decreases (see dashed blue line in Fig. 3). At $W_0 = W_c = 1.5$, $\kappa^- = 0$, $\kappa^+ > 0$, which means that the grating has a unidirectional coupling between different diffraction fields. We can find that $\kappa^+ > \kappa^- > 0$ for $W_0 < W_c$ and $\kappa^+ > 0, \kappa^- < 0$ for $W_0 > W_c$. In the two cases, the coupling constants satisfy $|\kappa^+| > |\kappa^-|$.

Then the total probe field $E_p(x,z)$ inside the grating region $0 \leqslant z \leqslant L$ is expressed in terms of multiple modes, each of which individually obeys Maxwell's equations and describes the diffraction amplitude along the corresponding diffraction order outside of the grating. Thus, the total field is given by

$$E_p(x,z) = \sum_{m=-\infty}^{+\infty} S_m(z)\, e^{-i(2\pi n_0 z/\lambda_p - mKx)}. \quad (26)$$

In the cases of $\lambda_p \ll \Lambda$ and a slow energy transfer between modes, both the second-order derivatives of the modes' amplitude, d^2S_m/dz^2, and the dephasing from the Bragg condition, S_m, are neglected. Consequently, the 1D Raman-Nath diffraction equation is obtained as

$$\frac{dS_m(z)}{dz} - i[\kappa^- S_{m+1}(z) + \kappa^+ S_{m-1}(z)] = 0. \quad (27)$$

On substituting the dimensionless coordinates $\xi = 2\pi n_1 z/\lambda_p$ into Eq. (27), we rewrite Eq. (27) as

$$\frac{dS_m(\xi)}{d\xi} - \frac{i}{2}[\sigma^- S_{m+1}(\xi) + \sigma^+ S_{m-1}(\xi)] = 0, \quad (28)$$

with $\sigma^{\pm} = 1 \pm n_2/n_1 = 1 \pm W_0/0.5V_0$.

For 2D atomic grating in the $\mathcal{PT}$-phase regime, the propagation constant $k_0 n(x,y)$ inside the atomic grating satisfies

$$\begin{aligned} k_0^2 n^2(x,y) = {} & \beta^2 - 2\beta[\kappa_x^+ \exp(iKx) + \kappa_x^- \exp(-iKx) \\ & + \kappa_y^+ \exp(iKy) + \kappa_y^- \exp(-iKy)], \end{aligned} \quad (29)$$

with

$$\kappa_x^{\pm} = \kappa_y^{\pm} = \frac{\pi(n_1 \pm n_2)}{\lambda_p} = \frac{0.0015\pi(0.5V_0 \pm W_0)}{2.383^{1/2}\lambda_p}, \quad (30)$$

where $\kappa_{x(y)}^+$ and $\kappa_{x(y)}^-$ are the strengths of the coupling along the positive and negative $x(y)$ directions, respectively. $\kappa_{x(y)}^+$ and $\kappa_{x(y)}^-$ have the similar change rule, with κ^+ and κ^- shown in Fig. 2.

The total probe field $E_p(x,y,z)$ inside the grating region $0 \leqslant z \leqslant L$ can be written as

$$E_p(x,y,z) = \sum_{m=-\infty}^{+\infty} \sum_{n=-\infty}^{+\infty} S_{(m,n)}(z) e^{-i(2\pi n_0 z/\lambda_p - mKx - nKy)}. \tag{31}$$

As a result, the Raman-Nath diffraction equation in two dimensions is given by

$$\frac{dS_{(m,n)}(z)}{dz} - i[\kappa_x^- S_{(m+1,n)}(z) + \kappa_x^+ S_{(m-1,n)}(z) + \kappa_y^- S_{(m,n+1)}(z) + \kappa_y^+ S_{(m,n-1)}(z)] = 0. \tag{32}$$

By substituting the dimensionless coordinates $\xi = 2\pi n_1 z/\lambda_p$, Eq. (32) can be rewritten as

$$\frac{dS_{(m,n)}(\xi)}{d\xi} - \frac{i}{2}[\sigma_x^- S_{(m+1,n)}(\xi) + \sigma_x^+ S_{(m-1,n)}(\xi) + \sigma_y^- S_{(m,n+1)}(\xi) + \sigma_y^+ S_{(m,n-1)}(\xi)] = 0, \tag{33}$$

with $\sigma_x^{\pm} = \sigma_y^{\pm} = 1 \pm n_2/n_1$.

We can acquire the diffraction efficiencies of different diffraction orders in one and two dimensions by solving the differential equations (28) and (33).

In the proposed scheme, we focus on showing the diffraction characteristics of the atomic grating in the Raman-Nath regime. However, Raman-Nath diffraction occurs when the condition

$$Q'\gamma \leqslant 1 \tag{34}$$

is satisfied [58]. If the probe field is normal incident, $Q' = 2\pi\lambda_p L/n_0\Lambda^2$ is the quality factor of the grating and $\gamma = \pi n_1 L/\lambda_p$ is the grating strength parameter.

III. RESULTS AND DISCUSSIONS

In this section, we focus on analyzing the Raman-Nath diffraction characteristics of 1D and 2D $\mathcal{PT}$-symmetric atomic gratings. Before presenting the numerical results, the maximum grating thickness $L_{\max}$ should be given by using the criterion of Raman-Nath regime diffraction in Eq. (34). When $V_0 = 3$ and $\Lambda = 20$ μm, $\varepsilon_0 = 2.383$ and $\varepsilon_1 = 0.0045$, which further lead to $L_{\max} = (\Lambda^2 n_0/2\pi^2 n_1)^{1/2} = (\Lambda^2\varepsilon_0/\pi^2\varepsilon_1)^{1/2} = 146.5$ μm. Thus, Raman-Nath diffraction theory is valid in the region $L \leqslant 146.5$ μm.

We first investigate the influence of the $\mathcal{PT}$-phase transition from an unbroken to broken $\mathcal{PT}$-phase regime on the distributions of Raman-Nath diffraction in one dimension. As we know, the nonzero balanced gain-absorption parameter W_0 can be used to tune the $\mathcal{PT}$ phase when V_0 is fixed to 3 [20,27]. We show in Fig. 4(a) the diffraction spectra of the 1D atomic grating as a function of $\sin\theta$ for three different values of W_0 by presenting the numerical results of Eq. (17). When the sinusoidal gain-absorption modulation exists, i.e., $W_0 \neq 0$, it is found from Fig. 4(a) that diffractions in all negative orders are suppressed and the asymmetric Raman-Nath diffraction phenomenon can be observed. Compared with the case of $W_0 = 0.35 < W_c$, the diffraction efficiencies of the grating in non-negative diffraction orders are greatly enhanced and the diffraction field of the -1st order also exists as $W_0 = 2.25 > W_c$. More interestingly, for the critical condition $W_0 = W_c = 1.5$, the diffraction fields in negative principal maxima are completely inhibited and only some extremely small diffraction side lobes exists [see the insets of Fig. 4(a)].

In order to present the asymmetric degree of the diffraction, we define a "diffraction ratio R," which is the intensity ratio of the -1st-order diffraction to the +1st-order diffraction:

$$R = \frac{I_{-1}}{I_{+1}} = \frac{I_p(\theta_{-1})}{I_p(\theta_{+1})}, \tag{35}$$

where I_{-1} and I_{+1} are obtained from Eq. (19). We plot the diffraction ratio R as a function of the gain-absorption parameter W_0 in Fig. 4(b). It is found that the diffraction ratio R first goes through exponential reduction as W_0 increases in the UPTP. At the EP (corresponding to $W_0 = 1.5$), the diffraction ratio R arrives at its minimum value $\sim 10^{-5.4}$ and can be regarded as $R = 0$. When W_0 increases from 1.5 to 2.5, which corresponds to BPTP, the diffraction ratio R starts to go through exponential growth. In other words, the lopsided Raman-Nath diffraction of 1D $\mathcal{PT}$-symmetric atomic grating can be realized at the EP.

In our model, the atomic grating with a $\mathcal{PT}$-symmetric optical potential can be considered as the superposition of an amplitude grating with sinusoidal gain-absorption modulation and a cosinusoidal-modulated phase grating. Consequently, the above interesting asymmetric diffraction phenomena, as shown in Fig. 4, originates from the interference between the amplitude grating and the phase grating [39,40]. For a periodically modulated grating, the amplitude transmission

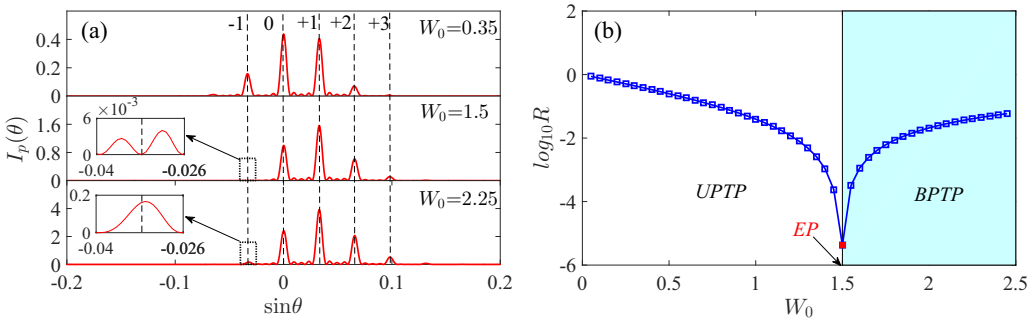

FIG. 4. (a) The Raman-Nath diffraction intensities as a function of $\sin\theta$ for different values of the gain-absorption parameter W_0. (b) The logarithm of diffraction ratio R, which describes the asymmetric degree of the diffraction, as a function of the parameter W_0. The insets in (a) show the diffraction in the -1st diffraction order. Other parameters are $V_0 = 3$, $N = 5$, and $L = 90$ μm.

function can be presented by a Fourier series development,

$$T(x) = \sum_n A_n \exp(inKx), \tag{36}$$

where $K = 2\pi/\Lambda$ and A_n stands for the amplitude of the nth diffraction order, which is obtained by the nth Fourier coefficient of the transmission function [from Eqs. (18) and (19)]:

$$A_n = \frac{1}{\Lambda}\int_0^{\Lambda} T(x)\exp(inKx)dx. \tag{37}$$

Thus, the diffraction spectrum $Q(\sin\theta)$ of the grating can be represented by a set of discrete values $\{A_n\}$ as

$$Q(\sin\theta) = \{A_n\} = \sum_n A_n \delta\left(\sin\theta - \frac{n\lambda_p}{\Lambda}\right). \tag{38}$$

For an amplitude grating with cosinusoidal modulation of the absorption and gain, the amplitude transmission function can be written as

$$T_1(x) = \exp[-\xi_1\cos(Kx)], \tag{39}$$

with $\xi_1 = 2\pi n_2 L/\lambda_p$.

The amplitudes of the diffraction orders diffracted by the amplitude grating are

$$\{B_n\} = \left\{(-1)^n I_n^B(\xi_1)\right\}, \tag{40}$$

where $I_n^B(\xi_1)$ is the nth-order modified Bessel function.

For a cosinusoidal phase grating, the amplitude transmission function is given by

$$T_2(x) = \exp[i\xi_2\cos(Kx)], \tag{41}$$

with $\xi_2 = 2\pi n_1 L/\lambda_p$.

The amplitudes of the diffraction orders diffracted by the phase grating are

$$\{C_n\} = \{(i)^n J_n(\xi_2)\}, \tag{42}$$

where $J_n(\xi_2)$ is the nth-order Bessel function of the first kind.

We can find from Eq. (16) that the transmission of the atomic grating is the product of the transmissions of an amplitude grating and a phase grating. Then the amplitude of each diffraction order of the atomic grating will be determined by a convolution operation of the diffracted amplitude series of both amplitude and phase gratings. Besides, there is a lateral $\pi/2$ phase shift between the amplitude and phase modulations of the $\mathcal{PT}$-symmetric atomic grating. Therefore, the diffraction amplitude of the atomic grating can be written as

$$\begin{aligned}\{A_n\} &= \left\{B_j \exp\left(-i\frac{j\pi}{2}\right)\right\} \otimes \{C_m\} \\ &= \left\{\sum_j B_j \exp\left(i\frac{-j\pi}{2}\right) C_{n-j}\right\},\end{aligned} \tag{43}$$

where $\otimes$ means the convolution operation.

The interference mechanism between the amplitude grating and phase grating of the $\mathcal{PT}$ grating can be illustrated by comparing the amplitudes of the ±1st diffraction orders. If the system parameters shown in Fig. 4 are selected, ξ_1 satisfies $0 < \xi_1 < 1.88$ so that $I_j^B(\xi_1)$ (for $|j| > 3$) can be neglected. Thus, the amplitudes of the ±1st diffraction orders can be calculated by using the convolution operation [Eq. (43)],

$$\begin{aligned}A_1 &= \sum_{j=-3}^{3} B_j C_{1-j} \\ &= B_{-3}C_4\exp\left(i\frac{3\pi}{2}\right) + B_{-2}C_3\exp(i\pi) \\ &\quad + B_{-1}C_2\exp\left(i\frac{\pi}{2}\right) + B_0C_1 + B_1C_0\exp\left(-i\frac{\pi}{2}\right) \\ &\quad + B_2C_{-1}\exp(-i\pi) + B_3C_{-2}\exp\left(-i\frac{3\pi}{2}\right) \\ &= i[\vartheta(\xi_1,\xi_2) + \tau(\xi_1,\xi_2)], \\ A_{-1} &= \sum_{j=-3}^{3} B_j C_{-1-j} \\ &= B_{-3}C_2\exp\left(i\frac{3\pi}{2}\right) + B_{-2}C_1\exp(i\pi) \\ &\quad + B_{-1}C_0\exp\left(i\frac{\pi}{2}\right) + B_0C_{-1} + B_1C_{-2}\exp\left(-i\frac{\pi}{2}\right) \\ &\quad + B_2C_{-3}\exp(-i\pi) + B_3C_{-4}\exp\left(-i\frac{3\pi}{2}\right) \\ &= i[\vartheta(\xi_1,\xi_2) - \tau(\xi_1,\xi_2)],\end{aligned} \tag{44}$$

where $\vartheta(\xi_1,\xi_2) = I_0^B(\xi_1)J_1(\xi_2) - I_2^B(\xi_1)J_1(\xi_2) + I_3^B(\xi_1)J_3(\xi_2)$ and $\tau(\xi_1,\xi_2) = I_1^B(\xi_1)J_0(\xi_2) + I_1^B(\xi_1)J_2(\xi_2) + I_3^B(\xi_1)J_2(\xi_2) + I_3^B(\xi_1)J_4(\xi_2)$.

According to Eq. (44), it is found that due to the lateral $\pi/2$ phase shift between sine-modulated gain-absorption and the cosine-modulated phase, the amplitude grating and the phase grating produce constructive interference in the diffraction direction of the $+1$st order and destructive interference in the -1st diffraction order. The constructive interference results in the $+1$st-order diffraction efficiency increasing, while the destructive interference leads to the diffraction efficiency of -1st order decreasing, which is the same for high diffraction orders $A_{\pm n}$ ($n \geqslant 2$). Therefore, we can observe an asymmetric diffraction spectrum shown in Fig. 4 for $\xi_1, \xi_2 > 0$, i.e., $W_0, V_0 > 0$. Especially for $\xi_1 = \xi_2 = \xi$ ($W_0 = 0.5V_0$), $\vartheta(\xi,\xi) = \tau(\xi,\xi)$ means that there is no diffraction in the -1st order. In other words, the lopsided diffraction spectra in Fig. 4 can indeed be achieved by the perfectly destructive interference between the amplitude and phase gratings in negative diffraction orders.

It has been found that the grating thickness can greatly influence the diffraction efficiencies of the atomic gratings [45–47,51]. In the following, we investigate the influence of the grating thickness on the Raman-Nath diffraction spectra for three different regions: EP, UPTP and BPTP. At the EP, the diffraction patterns as a function of $\sin\theta$ for three different grating thicknesses are plotted in Fig. 5(a). As shown in Fig. 5(a), in the Raman-Nath regime ($L \leqslant 146.5\ \mu$m), the increase of the thickness L stimulates higher-order diffraction fields in the positive-order direction and leads to a redistribution of the diffraction intensities in the positive orders. At the

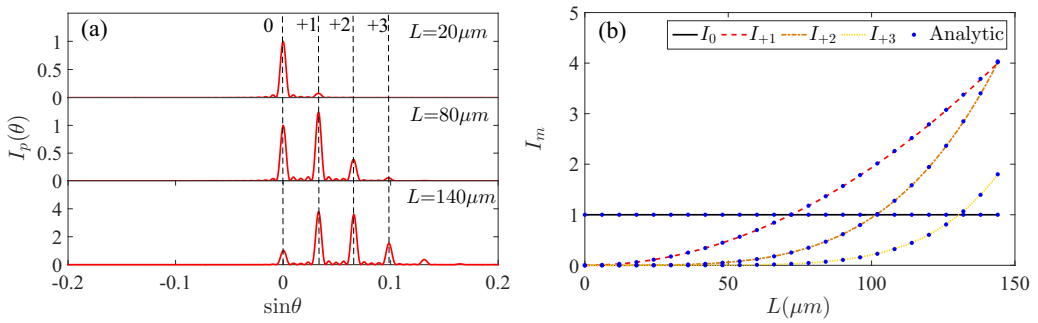

FIG. 5. (a) The Raman-Nath diffraction intensities as a function of $\sin\theta$ for different thicknesses of the atomic grating at EP. (b) The intensities of the corresponding diffraction orders in (a) as a function of the grating thickness L. Other parameters are the same as in Fig. 4.

phase-transition point, $\kappa^- = 0$ in the coupled-wave theory, resulting in $\sigma^- = 0$, means that there is no energy transformation from the S_{m+1} mode to the S_m mode. Besides, $\sigma^+ = 2$. Equation (28) then takes a simple form,

$$\frac{dS_m(\xi)}{d\xi} = iS_{m-1}(\xi). \tag{45}$$

By formally integrating Eq. (45), the solution for $S_m(\xi)$ can be obtained as

$$S_m(\xi) = i\int_0^{\xi} S_{m-1}(\xi')d\xi'. \tag{46}$$

It is obvious that all the modes $S_m(\xi)$ inside the grating satisfy the boundary conditions of $S_0(0) = 1$ and $S_m(0) = 0$ $(m \neq 0)$. Combining the boundary conditions with Eqs. (45) and (46), all negative diffractive orders are zero, i.e., $S_m(\xi) = 0$ $(m = -1, -2, \ldots)$, and the analytic solutions for the mth-order $(m = 0, +1, +2, \ldots)$ diffraction amplitude of 1D atomic grating at the EP are derived as

$$S_m(\xi) = i^m\frac{\xi^m}{m!}, \tag{47}$$

which further leads to the diffraction intensity $I_m = S_m S_m^*$ being written as

$$I_m(\xi) = \left(\frac{\xi^m}{m!}\right)^2. \tag{48}$$

In essence, the diffraction intensity I_m represents the corresponding diffraction efficiency because the incident field S_0 has a unit amplitude. By substituting $\xi = 2\pi n_1 L/\lambda_p$ into Eq. (39), we get the analytic expression of the diffraction efficiencies for the zeroth and first three positive diffraction orders in Eq. (48) as

$$I_0 = 1,\ I_{+1} = \frac{4\pi^2 n_1^2 L^2}{\lambda_p^2},\ I_{+2} = \frac{4\pi^4 n_1^4 L^4}{\lambda_p^4},$$
$$I_{+3} = \frac{16\pi^6 n_1^6 L^6}{9\lambda_p^6}, \tag{49}$$

with $n_1 = 0.00075V_0/2.383^{1/2}$.

Correspondingly, Fig. 5(b) plots the diffraction efficiencies for the zeroth and first three diffraction orders versus the grating thickness L. The result in Fig. 5(b) indicates that the numerical results match Eq. (49) well. Due to the coupling constant $\kappa^- = 0$ and the boundary condition $S_m(0) = \delta_{m0}$, the zeroth-order diffraction efficiency, i.e., $I_0(L) = 1$, is unaffected by the grating thickness L. Therefore, the atomic grating at the EP seems to be a transparent medium for the probe field. In addition, as shown in Figs. 5(a) and 5(b), the zero diffraction order dominates when $L < 72$ μm and then the diffraction efficiencies of the positive diffraction orders successively exceed 100% for $L > 72$ μm. Compared with the conventional atomic grating [39–42,44], the high-order diffraction efficiency can be greatly enhanced via increasing the grating thickness at the EP. Meanwhile, one can find from Figs. 5(a) and 5(b) that the total energy of the incident probe field is greater than that of the diffraction probe field, which means that the diffracted probe field can be amplified when

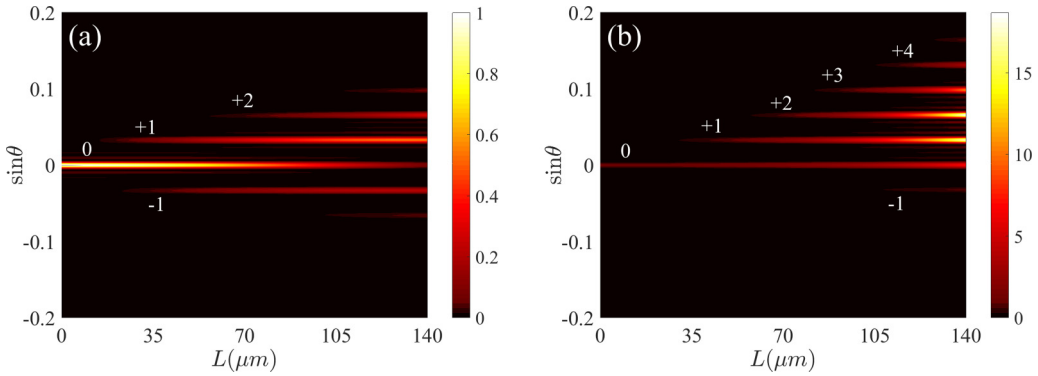

FIG. 6. The diffraction spectra of the atomic grating in the Raman-Nath regime as a function of the grating thickness L for (a) the unbroken PT -symmetric phase (UPTP) with $W_0 = 0.35 < 0.5V_0 = 1.5$ and (b) the broken PT -symmetric phase (BPTP) with $W_0 = 2.25 > 0.5V_0 = 1.5$. Other parameters are the same as in Fig. 4.

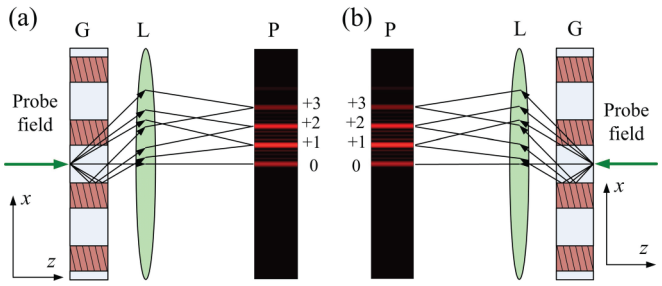

FIG. 7. The diffraction characteristics of the PT-symmetric atomic grating at the exceptional point (EP) for incidence from the (a) left side and the (b) right side. G: PT-symmetric atomic grating; L: convex lens; P: diffraction screen.

passing through the $\mathcal{PT}$-symmetric atomic grating. The gain of probe field comes from stimulated Raman gain process of the ^{85}Rb atomic system, which is pumped by an additional optical pumping laser field and driven by a control laser field. In this situation, the atomic population distribution satisfies $\rho_{cc}^{2(ss)} \gg \rho_{bb}^{2(ss)}$, Raman inversion takes place, and light amplification occurs from the stimulated Raman transition $|c,2\rangle \rightarrow |b,2\rangle$. That is to say, the additional optical pumping laser field and the control laser field provide energy to amplify the incident probe field.

Then we show the Raman-Nath diffraction spectra of the atomic grating as a function of the grating thickness L in the UPTP with $W_0 = 0.35$ and BPTP with $W_0 = 2.25$ in Fig. 6. In these two phase regions, the diffraction efficiencies in the positive diffraction orders could be enhanced as L increases. Meanwhile, the diffraction efficiency in the -1st order has a small improvement. Compared with the case at the EP shown in Fig. 5(b), one can find that the grating thickness has different roles on the zero-order diffraction efficiency for three different regions: UPTP, EP, and BPTP. More specifically, the zeroth-order diffraction efficiency can be decreased, unaffected, or improved with the increase of the grating thickness when the atomic grating is in the UPTP, at the EP, or in the BPTP.

In the laser-induced atomic grating, if the spatial distributions of the Stark field and control field remain unchanged, the spatial modulation of the refractive index along the x axis also remains the same. Whenever the probe field is incident into the grating from the left side (propagating along the $+z$ direction with wave vector k_z) or the right side (propagating along the $-z$ direction with wave vector $-k_z$), the optical lattice with a reciprocal lattice vector $K = 2\pi/\Lambda$ provides two transverse wave vectors for the probe field: a component $k_x = mK$ in the $+x$ direction and a component $k_{-x} = -mK$ in the $-x$ direction (m is a positive integer). For a 1D -symmetric optical lattice along the x axis, the reflection in the x axis from one end is zero, while it is enhanced from the other end at the EP [39]. That is to say, there is no reflection for the component $k_x = mK$ in the $+x$ direction in the condition of the complex refractive index $n(x) = n_0 - n_1[\cos(Kx) + i\sin(Kx)]$. Thus, the diffracted field is biased toward the $+x$ direction no matter whether it is incident into the atomic grating from the left side [see Fig. 7(a)] or the right side [see Fig. 7(b)]. In other words, the incident probe field is diffracted to non-negative diffraction orders for both left-side incident light and right-side incident light.

Let us now investigate the diffraction characteristics of 2D atomic grating with PT-symmetric optical potential in the Raman-Nath regime. Similar to the diffraction of 1D PT-symmetric grating, the gain-absorption parameter W_0 also plays an important role in the energy distribution of different diffraction orders of 2D atomic grating. Figure 8 shows 2D diffraction spectra for different values of the gain-absorption parameter W_0 in the Raman-Nath regime. Note that the 2D diffraction region can be divided into four domains: domain I ($0 \leqslant \sin\theta_x, \sin\theta_y \leqslant 1$), domain II ($-1 < \sin\theta_x < 0, 0 < \sin\theta_y < 1$), domain III ($-1 \leqslant \sin\theta_x, \sin\theta_y \leqslant 0$), and domain IV ($0 < \sin\theta_x < 1, -1 < \sin\theta_y < 0$). When $W_0 = 0.35 < W_c$, Raman-Nath diffraction of the atomic grating presents a 2D asymmetric diffraction spectrum, shown in Fig. 8(a). This is because 2D amplitude grating and 2D phase grating generate constructive interference in the diffraction orders of domain I and destructive interference in the diffraction orders of domains II–IV. Therefore, the diffraction in domain I is enhanced, while that in domains II–IV is suppressed. As shown in Fig. 8(b), in the case of $W_0 = W_c = 1.5$, the perfectly destructive interference results in the complete disappearance of the diffraction fields in domains II–IV and the realization of perfectly asymmetric diffraction. We can regard the perfectly asymmetric diffraction as 2D lopsided diffraction because all the diffraction fields only occur in the non-negative diffraction orders. As $W_0 = 2.25 > W_c$, the atomic grating is pushed into BPTP and the diffraction orders appear predominantly in domain I. However, some relative weak diffraction fields can also be observed in the other domains due to the imperfectly destructive interference [see Fig. 8(c)]. From Figs. 8(a)–8(c), it is clear that we can greatly improve the diffraction efficiencies

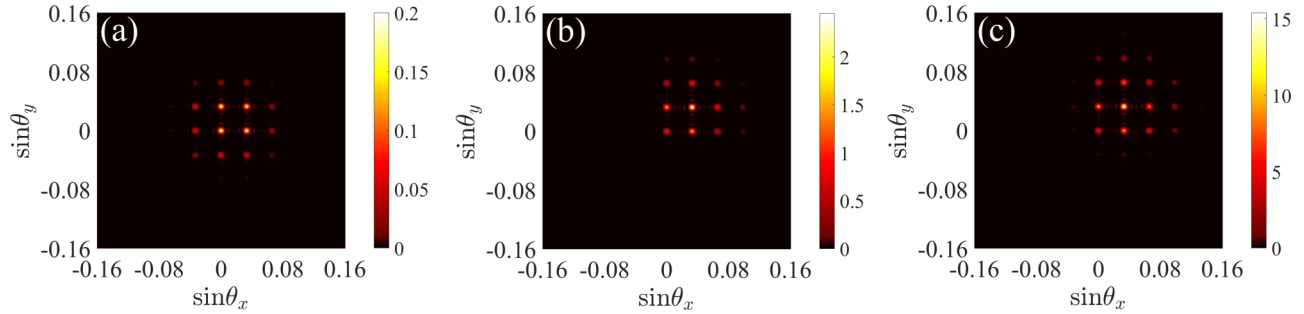

FIG. 8. The Raman-Nath diffraction intensities as a function of ($\sin\theta_x$, $\sin\theta_y$) for three values of the gain-loss parameter W_0: (a) $W_0 = 0.35$, (b) $W_0 = 1.5$, and (c) $W_0 = 2.25$. Other parameters are the same as in Fig. 4.

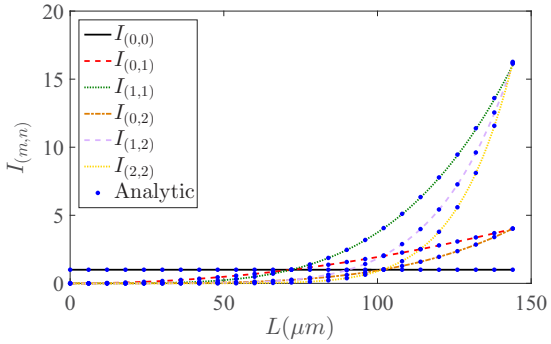

FIG. 9. The Raman-Nath diffraction intensities for some diffraction orders in domain I as a function of the grating thickness L. Other parameters are the same as in Fig. 4.

of the diffraction orders in domain I via adjusting the $\mathcal{PT}$ phase from an unbroken $\mathcal{PT}$-symmetric regime to a broken $\mathcal{PT}$-symmetric regime.

For the case that the 2D diffraction system is at the EP, $\sigma_x^- = \sigma_y^- = 0$ and $\sigma_x^+ = \sigma_y^+ = 2$; and then Eq. (33) is rewritten as

$$\frac{dS_{(m,n)}(\xi)}{d\xi} = i[S_{(m-1,n)}(\xi) + S_{(m,n-1)}(\xi)]. \tag{50}$$

Therefore, we can obtain the solution of $S_{(m,n)}(\xi)$ by integrating Eq. (41) as follows:

$$S_{(m,n)}(\xi) = i\int_0^{\xi} [S_{m-1,n}(\xi') + S_{m,n-1}(\xi')]d\xi'. \tag{51}$$

Note that the boundary conditions of $S_{(0,0)}(\xi) = 1$ and $S_{(m,n)}(\xi) = 0$ ($m \neq 0$ or $n \neq 0$) should be satisfied in 2D atomic grating with $\mathcal{PT}$-symmetric refractive index. For the cases of ($m = 0$, $n > 0$) or ($n = 0$, $m > 0$), one can find that Eq. (51) has the same expression with Eq. (37), which leads to $S_{(m,0)}(\xi) = S_{(0,m)}(\xi) = i^m\xi^m/m!$. Thus, $S_{(m,n)}(\xi) = S_{(n,m)}(\xi)$ is satisfied in domain I. The analytic expression of the diffraction efficiencies for the first six diffraction orders in domain I can be obtained as

$$I_{(0,0)} = 1, \quad I_{(0,1)} = \frac{4\pi^2 n_1^2 L^2}{\lambda_p^2}, \quad I_{(1,1)} = \frac{16\pi^4 n_1^4 L^4}{\lambda_p^4},$$
$$I_{(0,2)} = \frac{4\pi^4 n_1^4 L^4}{\lambda_p^4}, \quad I_{(1,2)} = \frac{16\pi^6 n_1^6 L^6}{\lambda_p^6}, \quad I_{(2,2)} = \frac{16\pi^8 n_1^8 L^8}{\lambda_p^8}, \tag{52}$$

with $n_1 = 0.00075V_0/2.383^{1/2}$.

The numerical and analytic solutions for the diffraction efficiencies in (0,0), (0,1), (1,0), (0,2), (1,2), and (2,0) diffraction orders of 2D atomic grating with $\mathcal{PT}$-symmetric refractive index at the EP are shown in Fig. 9. Our result illustrates that the coupled-wave analysis is valid to study Raman-Nath diffraction of 2D atomic grating. Figure 9 also shows that the (0,0)-order diffraction field is unaffected by the grating thickness when the probe field passes through 2D atomic grating at the EP, which is the same as 1D grating diffraction in Fig. 5(b). It is clear that the change of the grating thickness leads to a redistribution of the amplified diffraction fields in domain I (except the zeroth order). More interestingly, some diffractions fields in domain I have identical diffraction efficiencies for some particular values of the grating thickness.

In order to see more details, we present the diffraction spectra for three different grating thicknesses at the EP in Fig. 10. When the grating thickness has a small value, i.e., $L = 20$ μm, the atomic grating gathers the most probe energy in the (0,0) diffraction order and diffracts slight energy into the (0,1) and (1,0) orders, as shown in Fig. 10(a). As the thickness increases to 72 μm, some higher diffraction orders appears in domain I and the diffraction efficiencies of the (0,0), (0,1), (1,0), and (1,1) orders in domain I are all equal to 1, as shown in Fig. 10(b). In the case of $L = 102$ μm, as shown in Fig. 10(c), the (1,1)-order diffraction dominates and the diffraction efficiencies of the four adjacent diffraction orders are uniform. Therefore, we can accurately control the relative intensities of the diffraction fields in the Raman-Nath regime via adjusting the grating thickness when the probe field passes through 2D atomic grating at the EP.

IV. SUMMARY

In summary, we have theoretically investigated the diffraction characteristics of 1D and 2D atomic gratings with periodic $\mathcal{PT}$-symmetric refractive index in the Raman-Nath regime. In the proposed atomic system, the $\mathcal{PT}$-symmetric refractive index created by the interference of two Raman resonances can be continuously tuned via adjusting the spatial intensities of control and far-detuning Stark fields. It is demonstrated that the $\pi/2$ phase shift between the amplitude and phase gratings breaks the diffraction symmetry in the conventional atomic gratings [44–49] and generates the asymmetric diffraction effect. We give a suitable physical interpretation for the phenomenon of asymmetric diffraction via the interference of the amplitude and phase gratings in the Raman-Nath regime. At

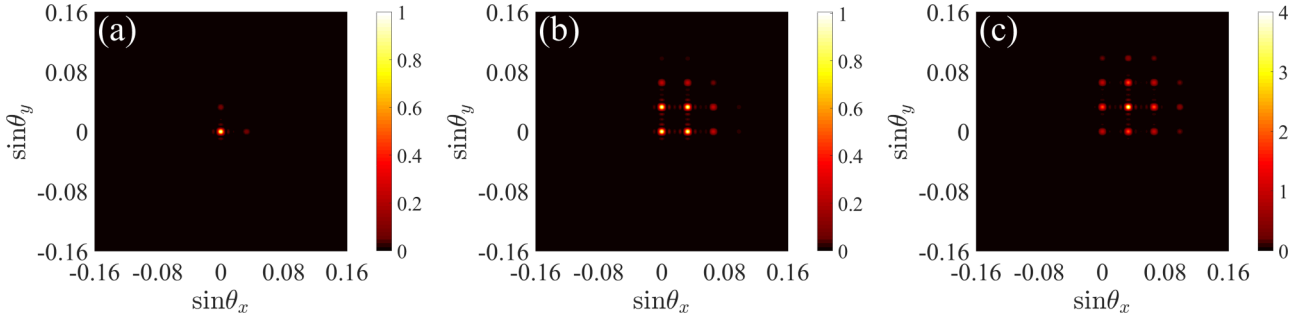

FIG. 10. The Raman-Nath diffraction intensities as a function of ($\sin\theta_x$, $\sin\theta_y$) for three different grating thicknesses L: (a) $L = 20$ μm, (b) $L = 72$ μm, and (c) $L = 102$ μm. Other parameters are the same as in Fig. 4.

the EP ($W_0 = W_c$), perfectly destructive interference exists in the 1D and 2D atomic gratings. As a result, the atomic gratings show a lopsided diffraction phenomenon, where the diffraction field only occurs in non-negative diffraction orders. Furthermore, we investigate the influence of the grating thickness on the Raman-Nath diffraction in different $\mathcal{PT}$-phase regions. It is found that some higher-order diffraction fields and a redistribution of the diffraction efficiencies in the Raman-Nath regime can be generated via increasing the grating thickness. More importantly, the zeroth-order diffraction field at the EP is unaffected by the change of the grating thickness. Our proposed scheme may be used to design a gain-beam splitter with tunable splitting ratio and other optical components in integrated optics.

ACKNOWLEDGMENTS

We would like to thank Professor Ren-Gang Wan for his encouragement and helpful discussions. The research is supported in part by the National Natural Science Foundation of China under Grants No. 11374050 and No. 11774054, and by the Natural Science Foundation of Jiangsu Province under Grant No. BK20161410.

APPENDIX: ARRANGEMENT FOR THE STARK AND CONTROL FIELDS

In order to construct the spatially refractive index with $\mathcal{PT}$ symmetry, we should give the arrangement for the Stark and control fields with spatial dependence.

For the 1D $\mathcal{PT}$-symmetric refractive index, the Stark field $E_S(x)$ and the control field $\Omega_c(x)$ are given by

$$\begin{aligned} E_S(x) &= E_{S0} + E_{S1}\cos(xk_S\sin\theta_S + \phi_{S1}) \\ &\quad + E_{S2}\cos(xk_S\sin\theta_S + \phi_{S2}), \\ &= E_{S0} + E_{S1}\cos(Kx + \phi_{S1}) \\ &\quad + E_{S2}\cos(Kx + \phi_{S2}), \\ \Omega_c(x) &= \Omega_{c0} + \Omega_{c1}\cos(xk_c\sin\theta_c + \phi_{c1}) \\ &\quad + \Omega_{c2}\cos(xk_c\sin\theta_c + \phi_{c2}), \\ &= \Omega_{c0} + \Omega_{c1}\cos(Kx + \phi_{c1}) \\ &\quad + \Omega_{c2}\cos(Kx + \phi_{c2}), \end{aligned} \tag{A1}$$

where $K = 2\pi/\Lambda = k_S\sin\theta_S = k_c\sin\theta_c$ and Λ is the period of the standing waves. ϕ_{ij} ($i = S,c$ and $j = 1,2$) is the initial phase of the corresponding standing wave. Note that $\Omega_{cj} = \vec{\mu}_{ac}\cdot\vec{e}_c E_{cj}/2\hbar$ ($j = 0,1,2$).

Based on the approach, i.e., numerical algorithm of the searching optimization, if taking $E_{S0} = (0.97 + 0.004V_0)E_0$, $E_{S1} = 0.004V_0E_0$, $E_{S2} = 0.021V_0E_0$, $\phi_{S1} = -\pi$, and $\phi_{S2} = -\pi/2$ with $E_0 = 10^4$V/cm for the Stark field $E_S(x)$ and $\Omega_{c0} = (2.553 - 0.001V_0)\Gamma$, $\Omega_{c1} = 0.001V_0\Gamma$, $\Omega_{c2} = 0.0032W_0\Gamma$, $\phi_{c1} = 0$, and $\phi_{c2} = \pi/2$ for the control field $\Omega_c(x)$, then we obtain

$$\begin{aligned} E_S(x)/E_0 &= 0.97 + 0.004V_0 - 0.004V_0\cos(Kx) \\ &\quad + 0.021W_0\sin(Kx), \\ \Omega_c(x)/\Gamma &= 2.553 - 0.001V_0 + 0.001V_0\cos(Kx) \\ &\quad - 0.032W_0\sin(Kx). \end{aligned} \tag{A2}$$

As a result, we can obtain 1D $\mathcal{PT}$-symmetric probe susceptibility, shown in Eq. (8), and a 1D $\mathcal{PT}$-symmetric refractive index, shown in Eq. (9).

For a 2D $\mathcal{PT}$-symmetric refractive index, the Stark field $E_s(x,y)$ and the control field $\Omega_c(x,y)$ are written as

$$\begin{aligned} E_S(x,y)/E_0 &= 0.97 + 0.008V_0 \\ &\quad - 0.004V_0[\cos(Kx) + \cos(Ky)] \\ &\quad + 0.021W_0[\sin(Kx) + \sin(Ky)], \\ \Omega_c(x,y)/\Gamma &= 2.553 - 0.002V_0 \\ &\quad + 0.001V_0[\cos(Kx) + \cos(Ky)] \\ &\quad - 0.032W_0[\sin(Kx) + \sin(Ky)], \end{aligned} \tag{A3}$$

when $E_{S0} = (0.97 + 0.008V_0)E_0$, $E_{S1} = E_{S3} = 0.004V_0E_0$, $E_{S2} = E_{S4} = 0.021V_0E_0$, $\phi_{S1} = \phi_{S3} = -\pi$, $\phi_{S2} = \phi_{S4} = -\pi/2$, $\Omega_{c0} = (2.553 - 0.002V_0)\Gamma$, $\Omega_{c1} = \Omega_{c3} = 0.001V_0\Gamma$, $\Omega_{c2} = \Omega_{c4} = 0.0032W_0\Gamma$, $\phi_{c1} = \phi_{c3} = 0$, and $\phi_{c2} = \phi_{c4} = \pi/2$. Consequently, 2D $\mathcal{PT}$-symmetric susceptibility, shown in Eq. (10), and the 2D $\mathcal{PT}$-symmetric refractive index, shown in Eq. (11), are achieved.

[1] C. M. Bender and S. Boettcher, Real spectra in Non-Hermitian Hamiltonians Having $\mathcal{PT}$ Symmetry, Phys. Rev. Lett. **80**, 5243 (1998).

[2] C. M. Bender, D. C. Brody, and H. F. Jones, Must a hamiltonian be hermitian, Am. J. Phys. **71**, 1095 (2003).

[3] R. El-Ganainy, K. G. Markris, D. N. Christodoulides, and Z. H. Musslimani, Theory of coupled optical $\mathcal{PT}$ symmetric structures, Opt. Lett. **32**, 2632 (2007).

[4] K. G. Makris, R. El-Ganainy, and D. N. Christodoulides, Beam Dynamics in $\mathcal{PT}$ Symmetric Optical Lattices, Phys. Rev. Lett. **100**, 103904 (2008).

[5] A. Guo, G. J. Salamo, D. Duchesne, R. Motandotti, M. Volatier-Ravat, V. Aimez, G. A. Siviloglou, and D. N. Christodoulides, Obesevation of $\mathcal{PT}$ -Symmetry Breaking in Complex Optical Potentials, Phys. Rev. Lett. **103**, 093902 (2009).

[6] S. Klaiman, U. Günther, and N. Moiseyev, Visualization of Branch Points in $\mathcal{PT}$ Symmetric Waveguides, Phys. Rev. Lett. **101**, 080402 (2008).

[7] C. E. Rüter, K. G. Makris, R. El-Ganainy, D. N. Christodoulides, M. Segev, and D. Kip, Observation of parity-time symmetry in optics, Nat. Phys. **6**, 192 (2010).

[8] H. Ramezani, T. Kottos, R. El-Ganainy, and D. N. Christodoulides, Unidirectional nonlinear $\mathcal{PT}$-symmetric optical structures, Phys. Rev. A **82**, 043803 (2010).

[9] P. A. Kalozoumis, C. V. Morfonios, F. K. Diakonos, and P. Schmelcher, $\mathcal{PT}$-symmetry breaking in waveguides with competing loss-gain pairs, Phys. Rev. A **93**, 063831 (2016).

[10] S. Longhi, Bloch Oscillation in Complex Crystals with $\mathcal{PT}$ Symmetry, Phys. Rev. Lett. **103**, 123601 (2009).

[11] Y. L. Xu, W. S. Fegadolli, L. Gan, M. H. Lu, X. P. Liu, Z. Y. Li, A. Scherer, and Y. F. Chen, Experimental realization of Bloch oscillations in a parity-time synthetic silicon photonic lattice, Nat. Commun. **7**, 11319 (2016).

[12] A. Szameit, M. C. Rechtsman, O. Bahat-Treidel, and M. Segev, $\mathcal{PT}$-symmetry in honeycomb photonic lattices, Phys. Rev. A **84**, 021806(R) (2011).

[13] S. Longhi, Non-reciprocal transmission in photonic lattices based on unidirectional coherent perfect absorption, Opt. Lett. **40**, 1278 (2015).

[14] L. Chang, X. Jiang, S. Hua, C. Yang, J. Wen, L. Jiang, G. Li, G. Wang, and M. Xiao, Parity-time symmetry and variable optical isolation in active-passive-coupled mocroresonators, Nat. Photon. **8**, 524 (2014).

[15] L. Feng, Z. J. Wong, R. M. Ma, Y. Wang, and X. Zhang, Single-mode laser by parity-time symmetry breaking, Science **346**, 972 (2014).

[16] X. Y. Lü, H. Jing, J. Y. Ma, and Y. Wu, $\mathcal{PT}$-Symmetry-Breaking Chaos in Optomechanics, Phys. Rev. Lett. **114**, 253601 (2015).

[17] J. Li, R. Yu, C. Ding, and Y. Wu, $\mathcal{PT}$-symmetry-induced evolution of sharp asymmetric line shapes and high-sensitivity refractive index sensors in a three-cavity array, Phys. Rev. A **93**, 023814 (2016).

[18] J. Li, J. Li, Q. Xiao, and Y. Wu, Giant enhancement of optical high-order sideband generation and their control in a dimer of two cavities with gain and loss, Phys. Rev. A **93**, 063814 (2016).

[19] W. X. Yang, A. X. Chen, X. T. Xie, and L. Ni, Enhanced generation of higher-order sidebands in a single-quantum-dot-cavity system coupled to a $\mathcal{PT}$-symmetric double cavity, Phys. Rev. A **96**, 013802 (2017).

[20] C. Hang, G. X. Huang, and V. V. Konotop, $\mathcal{PT}$ Symmetry with a System of Three-Level Atoms, Phys. Rev. Lett. **110**, 083604 (2013).

[21] C. Hang and G. X. Huang, Weak-light solitons and their active control in a parity-time-symmetric atomic system, Phys. Rev. A **91**, 043833 (2015).

[22] C. Hang, G. X. Huang, and V. V. Konotop, Tunable spectral singularities: Coherent perfect absorber and laser in an atomic medium, New. J. Phys. **18**, 085003 (2016).

[23] J. Sheng, M. A. Miri, D. N. Christodoulides, and M. Xiao, PT-symmetric optical potentials in a coherent atomic medium, Phys. Rev. A **88**, 041803(R) (2013).

[24] Z. Y. Zhang, Y. Q. Zhang, J. T. Sheng, L. Yang, M. A. Miri, D. N. Christodoulides, B. He, Y. P. Zhang, and M. Xiao, Observation of Parity-Time Symmetry in Optically Induced Atomic Lattices, Phys. Rev. Lett. **117**, 123601 (2016).

[25] Ziauddin, Y. L. Chuang, and R. K. Lee, Gaint Goos-Hanchen shift using $\mathcal{PT}$ symmetry, Phys. Rev. A **92**, 013815 (2015).

[26] Z. Lin, H. Ramezani, T. Eichelkraut, T. Kottos, H. Cao, and D. N. Christodoulides, Unidirectional Invisibility Induced by $\mathcal{PT}$-Symmetric Periodic Structures, Phys. Rev. Lett. **106**, 213901 (2011).

[27] L. Feng, M. Ayache, J. Q. Huang, Y. L. Xu, M. H. Lu, Y. F. Chen, Y. Fainman, and A. Scherer, Nonreciprocal light propagation in a silicon photonic circuit, Science **333**, 729 (2011).

[28] S. Longhi, Spectral singularities and Bragg scattering in complex crystals, Phys. Rev. A **81**, 022102 (2010).

[29] M. Kulishov, H. F. Jones, and B. Kress, Analysis of PT-symmetric volume grating beyond the paraxial approximation, Opt. Express **23**, 9347 (2015).

[30] X. Y. Zhu, Y. L. Xu, Y. Zou, X. C. Sun, C. He, M. H. Lu, X. P. Liu, and Y. F. Chen, Asymmetric diffraction based on a passive parity-time grating, Appl. Phys. Lett. **109**, 111101 (2016).

[31] V. A. Bushuev, L. V. Dergacheva, and B. I. Mantsyzov, Asymmetric pendulum effect and transparency change of $\mathcal{PT}$-symmetric photonic crystals under dynamical Bragg diffraction beyond the paraxial approximation, Phys. Rev. A **95**, 033843 (2017).

[32] C. Palmer, and E. Loewen, *Diffraction Grating Handbook* (Newport Corp., Rochester, New York, 2005).

[33] T. K. Gaylord and M. G. Moharam, Analysis and applications of optical diffraction by gratings, Proc. IEEE **73**, 894 (1985).

[34] B. Wang, C. Zhou, S. Wang, and J. Feng, Polarizing beam splitter of a deep-etched fused-silica grating, Opt. Lett. **32**, 1299 (2007).

[35] D. Fattal, J. Li, Z. Peng, M. Fiorentino, and R. G. Beausoleil, Flat dielectric grating reflectors with focusing abilities, Nat. Photon. **4**, 466 (2010).

[36] M. Khorasaninejad and F. Capasso, Broadband multifunctional efficient meta-grating based on dielectric waveguide phase shifters, Nano Lett. **15**, 6709 (2015).

[37] R. B. Witmer and J. M. Cork, The measurement of x-ray emission wave-length by means of the ruled grating, Phys. Rev. **42**, 743 (1932).

[38] H. Kogelnik, Coupled wave theory for thick hologram grating, Bell Syst. Tech. J. **48**, 2909 (1969).

[39] L. Song, R. A. Lessard, and P. Galarneau, Diffraction efficiency of a thin amplitude-phase holographic grating: A convolution approach, J. Mod. Opt. **37**, 1319 (1990).

[40] A. Granger, L. Song, and R. A. Lessard, Multiple beam generation using a stratified volume holographic grating, Appl. Opt. **32**, 2534 (1993).

[41] G. G. Zakharyan and A. V. Galstyan, Mixed phase and absorption thin grating diffraction, Opto-Electron. Rev. **15**, 20 (2007).

[42] M. B. Sobnack, W. C. Tan, N. P. Wanstall, T. W. Preist, and J. R. Sambles, Stationary Surface Plasmons on a Zero-Order Metal Grating, Phys. Rev. Lett. **80**, 5667 (1998).

[43] Y. Wu and X. Yang, Electromagnetically induced transparency in V-, Λ-, and cascade-type schemes beyond steady-state analysis, Phys. Rev. A **71**, 053806 (2005).

[44] H. Y. Ling, Y. Q. Li, and M. Xiao, Electromagnetically induced grating: Homogeneously broadened medium, Phys. Rev. A **57**, 1338 (1998).

[45] L. E. E. de Araujo, Electromagnetically induced phase grating, Opt. Lett. **35**, 977 (2010).

[46] S. Q. Kuang, C. S. Jin, and C. Li, Gain-phase grating based on spatial modulation of active Raman gain in cold atoms, Phys. Rev. A **84**, 033831 (2011).

[47] R. G. Wan, J. Kou, L. Jiang, Y. Jiang, and J. Y. Gao, Electromagnetically induced grating via enhanced nonlinear modulation by spontaneously generated coherence, Phys. Rev. A **83**, 033824 (2011).

[48] G. L. Cheng and A. X. Chen, Squeezing induced high-efficiency diffraction grating in two-level system, Opt. Express **25**, 4483 (2017).

[49] L. Wang, F. Zhou, P. Hu, Y. Niu, and S. Gong, Two-dimensional electromagnetically induced cross-grating in a four-level tripod-type atomic system, J. Phys. B **47**, 225501 (2014).

[50] L. Zhao, W. Duan, and S. F. Yelin, Generation of tunable-volume transmission-holographic gratings at low light levels, Phys. Rev. A **84**, 033806 (2011).

[51] S. A. Carvalho and L. E. E. de Araujo, Electromagnetically - induced phase grating: A coupled-wave theory analysis, Opt. Express **19**, 1936 (2011).

[52] M. Mitsunaga and N. Imoto, Observation of an electromagnetically induced grating in cold sodium atoms, Phys. Rev. A **59**, 4773 (1999).

[53] A. W. Brown and M. Xiao, All-optical switching and routing based on an electromagnetically induced absorption grating, Opt. Lett. **30**, 699 (2005).

[54] L. Zhao, W. Duan, and S. F. Yelin, All-optical beam control with high speed using image-induced blazed gratings in coherent media, Phys. Rev. A **82**, 013809 (2010).

[55] W. Kleemann and J. Ferré, Bragg-regime diffraction and waveguiding of light by ferromagnetic domains in K_2CuF_4, Phys. Rev. B **24**, 1568 (1981).

[56] C. Neipp, I. Pascual, and A. Beléndez, Experimental evidence of mixed gratings with a phase difference between the phase and amplitude grating in volume holograms, Opt. Express **10**, 1374 (2002).

[57] W. A. Riley, J. Alan love, and D. W. Griffith, Observation of Raman-Nath optical diffraction in the phase grating plane, J. Acoust. Soc. Am. **71**, 1149 (1980).

[58] T. K. Gaylord and M. G. Moharam, Thin and thick gratings: Terminology clarification, Appl. Opt. **20**, 3271 (1981).

[59] D. A. Steck, Rubidium 85 D line data, Rubidium 87 D line data, available online at http://steck.us/alkalidata.

[60] N. A. Proite, B. E. Unks, J. T. Green, and D. D. Yavuz, Refractive Index Enhancement with Vanishing Absorption in an Atomic Vapor, Phys. Rev. Lett. **101**, 147401 (2008).

[61] D. D. Yavuz, Refractive Index Enhancement in a Far-Off Resonant Atomic System, Phys. Rev. Lett. **95**, 223601 (2005).

[62] C. O'Brien, P. M. Anisimov, Y. Rostovtsev, and O. Kocharovskaya, Coherent control of refractive index in far-detuned systems, Phys. Rev. A **84**, 063835 (2011).

[63] Y. Bai, N. bandyopadhayay, S. Tsao, S. Slivken, and M. Razeghi, Room temperature quantum cascade lasers with 27% wall plug efficiency, Appl. Phys. Lett. **98**, 181102 (2011).